Contents lists available at ScienceDirect

Journal of Saudi Chemical Society

journal homepage: www.ksu.edu.sa

Novel magnetically separable g-C_3N_4/TiO_2/$CuFe_2O_4$ photocatalyst for efficient degradation of tetracycline under visible light irradiation: Optimization of process by RSM

Khalid Mujasam Batoo [a], Kadhim Hussein Jassim [b], Talal Aziz Qassem [c,*], Sajjad Hussain [d,e], Wafaa Talib Hasson [f], Sarah Salah Jalal [g], Montather F. Ramadan [h], Safaa Mustafa Hameed [i], Ahmed Hussien Alawadi [j,k,l], Ali Alsaalamy [m]

[a] College of Science, King Saud University, P.O. Box-2455, Riyadh 11451, Saudi Arabia
[b] Nursing College, Al-Mustaqbal University, 51001 Hillah, Babylon, Iraq
[c] Department of Medical Laboratory Technics, Al-Noor University College, Nineveh, Iraq
[d] Hybrid Materials Center (HMC), Sejong University, Seoul 05006, Republic of Korea
[e] Department of Nanotechnology and Advanced Materials Engineering, Sejong University, Seoul 05006, Republic of Korea
[f] Department of Medical Laboratory Technics, Al-Hadi University College, Baghdad 10011, Iraq
[g] College of Pharmacy, National University of Science and Technology, Dhi Qar, Iraq
[h] College of Dentistry, Al-Ayen University, Thi-Qar, Iraq
[i] Department of Optics, College of Health & Medical Technology, Sawa University, Almuthana, Iraq
[j] College of Technical Engineering, the Islamic University, Najaf, Iraq
[k] College of Technical Engineering, the Islamic University of Al Diwaniyah, Iraq
[l] College of Technical Engineering, the Islamic University of Babylon, Iraq
[m] College of Technical Engineering, Imam Ja'afar Al-Sadiq University, Al-Muthanna 66002, Iraq

ARTICLE INFO

Keywords:
g-C_3N_4/TiO_2/$CuFe_2O_4$ heterostructure
Magnetic nanocomposite
TC degradation
Photocatalyst
Response surface methodology

ABSTRACT

Herein, a novel magnetic visible-driven g-C_3N_4/TiO_2/$CuFe_2O_4$ nanocomposite with excellent photocatalytic performance was successfully prepared and employed for photodegradation of tetracycline. Several analysis including X-Ray diffraction (XRD), Fourier Transform Infrared Spectroscopy (FTIR), Field Emission Scanning Electron Microscopy (FESEM), energy dispersive X-ray (EDX), Vibrating-Sample Magnetometer (VSM), and Ultraviolet–Visible Diffuse Reflectance Spectroscopy (UV–Vis DRS) were performed in order to study the structural, optical, magnetic, as well as morphological properties of nanocomposite. The optical band gap of g-C_3N_4/TiO_2/$CuFe_2O_4$ heterostructure was found to be red shifted to 2.45 eV from 3.15 eV for pure TiO_2. Enhanced separation of photoinduced electron-hole pairs and enhanced visible light absorption capacity of nanocomposite lead to a maximum tetracycline photodegradation efficiency. Response surface methodology (RSM) was used to investigate the influence four independent variables, including initial photocatalyst dosage (7–14 g/L), TC concentration (20–30 ppm), solution pH (5.5–7.5), and irradiation time (20–40 min), and optimize the TC degradation efficiency. The g-C_3N_4/TiO_2/$CuFe_2O_4$ nanocomposite was able to separate and recycle easily using an external magnetic field, and the results of reusability was shown its high stability after 5 cycles. Active species trapping experiments suggested that holes and hydroxyl radicals played a crucial role in the TC degradation process. Finally, a potential photocatalytic mechanism for photodegradation of TC was proposed.

1. Introduction

The pollution of water with pharmaceutical antibiotics such as tetracycline (TC) has attracted much attention due to their poor metabolism, high chemical stability, and high water-solubility [1]. These pollutants even in the low concentration can lead to serious problems such as drug resistance and chronic toxicity, which is a considerable threat for human health and aquatic environment [2,3]. Therefore, the eliminating of such pollutants from wastewater is highly desirable. A variety of water purification techniques such as biodegradation [4],

* Corresponding author.
E-mail address: talal.aziz@alnoor.edu.iq (T.A. Qassem).

https://doi.org/10.1016/j.jscs.2024.101871
Received 23 August 2023; Received in revised form 24 April 2024; Accepted 30 April 2024
Available online 1 May 2024

chlorination [5], flocculation [6], and adsorption [7,8,9] have been used for eliminating these toxic pollutants. Although somewhat efficient, the application of these techniques is limited due to numerous shortcomings such as generation byproducts, high cost, time-consuming, and incomplete elimination. To solve these drawbacks, advanced oxidation processes (AOPs), which use reactive oxygen species to remove the pollutants have been attracted more attention [10,11]. Photocatalyst based semiconductors are one of the most efficient AOPs techniques for wastewater treatment, due to their high efficiency and utilize solar energy directly [12–15].

TiO_2 have been regarded as the promising photocatalyst material for removal of pollutants from aqueous solution because of its high stability, nontoxicity, excellent physicochemical properties, and low-cost [16,17]. However, its performance is hindered by the wide band gap energy and rapid recombination of photoinduced carriers [18,19]. Hence, numerous methodologies have been developed to improve sun ligth photocatalytic performance of TiO_2. One of the promising strategy is coupling of TiO_2 with other semiconductors and the construction of heterojunction nanocomposites [20–22]. Among these semiconductor materials, graphitic carbon nitride (g-C_3N_4) is commonly used owning to its nontoxicity, narrow band gap, cost-effectiveness, and high stability [23,24]. These interesting properties make g-C_3N_4 very useful in various field of science such as solar cell [25], chemical sensors [26], and photoelectronic [27], and photocatalyst [28–30]. Nevertheless, the photocatalytic functionality of pure g-C_3N_4 is hindered by the rapid recombination kinetics of photoexcited charge carriers, alongside its restricted surface area. These constraints impede the material's overall photocatalytic efficiency, necessitating further enhancement strategies to optimize its performance in catalytic applications. Gündoğmuş et al. prepared TiO_2/g-C_3N_4 heterojunction through one pot hydrothermal procedure, which exhibited superb photodegradation performance to methylene blue dye under irradiation of visible light [31]. Preparation and application of magnetic photocatalysts with interesting properties such as fast separation, low cost, and basic technical necessities are promising procedure in the wastewater treatment [32]. Thus, the photocatalysts can be coupled with magnetic nanoparticles to facilitate separation.

Recently, the spinel ferrite structure (MFe_2O_4 like $CuFe_2O_4$, $MnFe_2O_4$, and $CoFe_2O_4$, etc.) photocatalysts were widely explored to degradation of organic pollutants. Among them, copper ferrite ($CuFe_2O_4$) has been demonstrated as a promising ferromagnetic materials, as it possess many advantages such as simple preparation, high chemical and thermal stability, low toxicity, narrow band gap, low cost, and fascinating magnetically separable properties [33,34]. Therefore, the coupling $CuFe_2O_4$ with other materials provides an efficient and convenient strategy for increased visible-light photocatalytic performance, which can be easily separated using magnetic field. Atacan and co-workers were synthesized $CuFe_2O_4$/MoS_2 p-n heterojunction and used for photodegradation of Rhodamine B [35]. The synthesized magnetic nanocomposite was shown excellent photocatalytic performance and reusability.

In this research, we reported preparation of a novel magnetic recoverable g-C_3N_4/TiO_2/$CuFe_2O_4$ nanocomposite by a simple wet impregnation procedure. The as-prepared materials were characterized by different analyses such as XRD, FT-IR, FESEM, EDX, VSM, and UV–vis DRS. The photocatalytic activity of the as-fabricated nanocomposite was evaluated using studying the photodegradation of TC and shown photoinduced increased photocatalytic activity. Besides, the effect of TC concentration, photocatalyst dosage, time of irradiation, and solution pH on the photodegradation process were investigated using response surface methodology (RSM). The as-prepared nanocomposite exhibited good reusability against TC for continuous cyclic runs. Scavenging experiments was then used to identify primarily reactive species. Furthermore, the possible degradation pathway of TC by g-C_3N_4/TiO_2/$CuFe_2O_4$ nanocomposite was investigated in detail.

2. Experimental

2.1. Chemicals and reagents

Titanium (IV) isopropoxide (TTIP), melamine ($C_3H_6N_6$), cupper nitrate trihydrate ($Cu(NO_3)_2{\cdot}3H_2O$), Iron (III) nitrate nonahydrate ($Fe(NO_3)_3{\cdot}9H_2O$), isopropanol (C_3H_8O), sodium hydroxide (NaOH), nitric acid (HNO_3), and methanol (CH_3OH) were the reagents which used for synthesis TiO_2, g-C_3N_4, $CuFe_2O_4$, g-C_3N_4/TiO_2/$CuFe_2O_4$ nanocomposite. All the reagents were applied without further purification.

2.2. Synthesis of TiO_2

The TiO_2 nanoparticles were prepared through hydrolyze and peptization of TTIP solution according to the reported procedures. Briefly, 5 mL TTIP and 15 mL isopropanol were slowly added to 250 mL of distilled water (pH = 3, adjusted by adding HNO_3). The mixture was magnetically stirred at room temperature for 3 h, and after that kept at 70 °C for 22 h in an oven. Finally, the resulted product was separated by centrifugation and dried at 70 °C, after which the sample was calcinated or annealed at 400 °C for 2 h.

2.3. Synthesis of g-C_3N_4

For preparation of g-C_3N_4 nanosheets at first a certain amount of melamine was put in a crucible and heated at 550 °C for 4 h in a muffle furnace. Then, the resultant yellow sample grounded and ultrasonicated in methanol for 30 min. Finally, the product was washed with distilled water and dried at 65 °C for 12 h.

2.4. Synthesis of $CuFe_2O_4$

Magnetic $CuFe_2O_4$ nanoparticles was prepared by co-precipitation procedure [36]. Typically, 5 mmol $Fe(NO_3)_3{\cdot}9H_2O$, and 2.5 mmol $Cu(NO_3)_2{\cdot}3H_2O$ were dissolved in distilled water (100 mL) magnetically stirring. After that, 75 mL NaOH (4 M) was slowly dropped into the obtained mixture and kept at 90 °C for 2 h. The obtained magnetic $CuFe_2O_4$ nanoparticles were collected by an external magnet, washed with distilled water, and finally dried at 75 °C.

2.5. Synthesis of TiO_2/g-C_3N_4/$CuFe_2O_4$

TiO_2/g-C_3N_4/$CuFe_2O_4$ was prepared using a simple wet impregnation procedure. The equal weight ratio (1:1:1) of TiO_2, g-C_3N_4, and $CuFe_2O_4$ were dispersed in 30 mL EtOH individually, ultrasonicated for 30 min, and then mixed together. The obtained mixture was magnetically stirred for 24 h. Finally, the obtained magnetic nanocomposite were isolated by external magnet, and dried at 80 °C.

2.6. Characterization techniques

The crystal structure and phase purity of the as-prepared samples were analyzed by XRD technique on an MACSCIENCE MXP3 diffractometer under Cu Kα radiation. The surface functional group of the as-synthesized samples were obtained using a Nicolet Avatar 370 spectrometer. Using a ZEISS SIGMA VP scanning electron microscope, the samples went through FESEM and EDS analyses to study their surface morphology, elemental constitution, and distribution. JASCO V-65 spectrophotometer was used to record the UV–visible absorption and diffuse reflectance (DRS) spectra of the as-prepared samples. The magnetic properties of the as-prepared g-C_3N_4/TiO_2/$CuFe_2O_4$ nanocomposite were analyzed with Lakeshore VSM 7410 magnetometer.

2.7. Assessment of photocatalytic activity

The photocatalytic performance of the as-synthesized samples were

Table 1
Range and level values of independent variables.

Parameter	Code	Real values				
		−α	−1	0	+1	+α
Dosage (mg)	A	3.5	7.0	10.5	14.0	17.5
Initial concentration (ppm)	B	15	20	25	30	35
Contact time (min)	C	10	20	30	40	50
pH	D	4.5	5.5	6.5	7.5	8.5

Table 2
Design of experiments matrix along with experimental values of removal percentage of TC by the g-C_3N_4/TiO_2/$CuFe_2O_4$.

Run	A (mg)	B (ppm)	C (min)	D:pH	%R
1	10.5	25	30	8.5	73.26
2	14	30	20	5.5	84.26
3	10.5	25	30	6.5	67.21
4	7	30	40	7.5	70.12
5	10.5	15	30	6.5	91.28
6	10.5	25	30	6.5	60.18
7	10.5	25	30	6.5	62.29
8	7	20	20	7.5	69.51
9	7	20	40	7.5	77.81
10	7	20	40	5.5	86.51
11	7	30	20	5.5	70.12
12	3.5	25	30	6.5	59.68
13	10.5	35	30	6.5	72.25
14	10.5	25	30	4.5	91.02
15	10.5	25	30	6.5	63.18
16	14	30	20	7.5	76.02
17	10.5	25	10	6.5	68.12
18	14	20	40	5.5	98.42
19	7	30	20	7.5	65.13
20	14	20	40	7.5	90.08
21	14	20	20	7.5	83.25
22	14	30	40	5.5	90.09
23	14	30	40	7.5	82.18
24	10.5	25	30	6.5	61.89
25	7	30	40	5.5	77.99
26	17.5	25	30	6.5	89.11
27	10.5	25	50	6.5	85.18
28	7	20	20	5.5	77.81
29	14	20	20	5.5	92.31
30	10.5	25	30	6.5	64.05

investigated using photodegradation of TC under irradiation of visible light using LED lamp. In a typical procedure, a certain quantities of photocatalyst was dispersed into TC solution with desired concentration, and then stirred in the dark for 30 min to get adsorption/desorption equilibrium. Then, the suspension was exposed to visible light for a specific time. The residual concentration of TC was quantified through the utilization of UV–visible spectrophotometry (λ_{max} = 365 nm).

2.8. Experimental design

In order to evaluate the effects of key experimental variables on the degradation efficiency and also optimize the photocatalytic process, RSM based central composite design (CCD) was performed. Design Expert 10 software was used to design of experimental. In this research, four key variables containing dosage of g-C_3N_4/TiO_2/$CuFe_2O_4$ (mg, A), initial concentration of TC (mg.L^{-1}, B), irradiation time (min, C), and solution pH (D) were considered as significant experimental variables affecting the photocatalytic performance. Table 1 was listed the ranges and levels of the four selected operational variables. Based on CCD-RSM a set of 30 experiment were conducted and the obtained matrix was shown in Table 2.

3. Results and discussion

3.1. Characterization of photocatalyst

The XRD crystalline patterns of TiO_2, g-C_3N_4, $CuFe_2O_4$, and g-C_3N_4/TiO_2/$CuFe_2O_4$ nanocomposite were depicted in Fig. 1a. The pattern of TiO_2 was shown diffraction peaks at 2θ = 25.55°, 37.94°, 48.28°, 55.0°, 63.10°, 70.02°,and 75.6° with corresponding hkl planes of (101), (004), (200), (211), (204), (220), and (215), respectively, which was well matched with anatase phase of TiO_2 (JCPDS No. 00-021-1272). For pure g-C_3N_4, the diffraction peaks at 2θ = 13.07° and 27.72° were correspond to the (100), and (002) plans (JCPDS No. 87-1526). Furthermore, the XRD pattern of $CuFe_2O_4$ was displayed peaks at 2θ of 18.5°, 30.2°, 35.8°, 43.03°, 57.05° and 62.8°, which are related to (111), (220), (311), (400), (511) and (440) planes, respectively. These reflections are agree well with spinel cubic phase of $CuFe_2O_4$ (JCPDS No. 25-0283).The characteristic peaks of TiO_2, g-C_3N_4, and $CuFe_2O_4$ coexisted in the pattern of g-C_3N_4/TiO_2/$CuFe_2O_4$ nanocomposite, which confirm the TiO_2, and $CuFe_2O_4$ were successfully anchored on the surface of g-C_3N_4 nanosheets. Furthermore, in the XRD pattern of g-C_3N_4/TiO_2/$CuFe_2O_4$ nanocomposite no additional diffraction peaks were observed, which confirm the phase purity of the nanocomposite. Thus, TiO_2, g-C_3N_4, and $CuFe_2O_4$ coexist stably in the ternary heterojunction without chemical reaction. In addition the XRD patterns

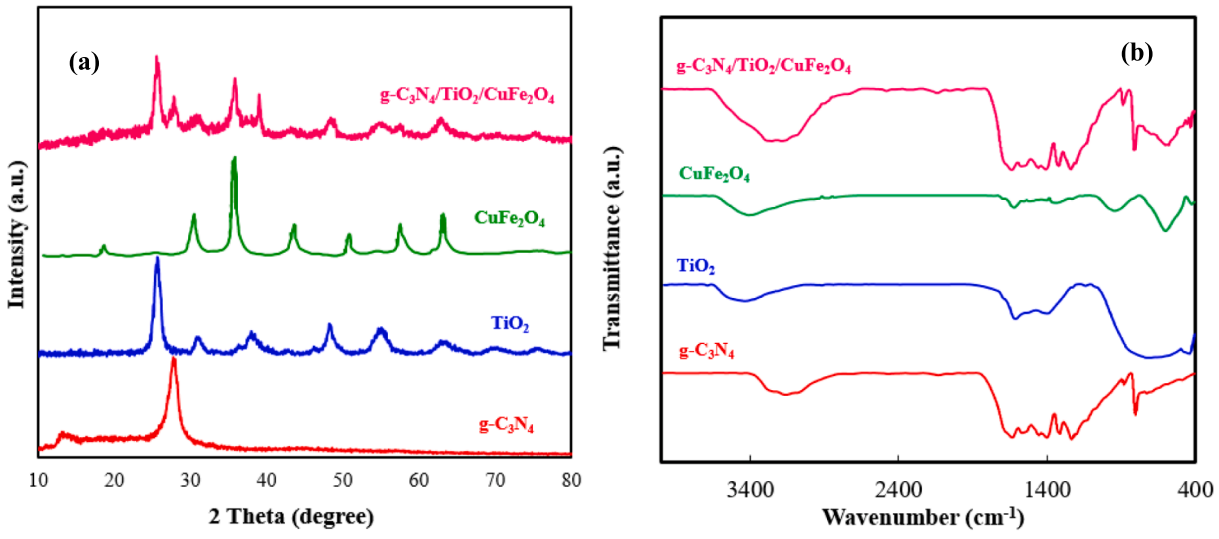

Fig. 1. XRD patterns (a), and FTIR spectra (b) of g-C_3N_4, TiO_2, $CuFe_2O_4$, and g-C_3N_4/TiO_2/$CuFe_2O_4$ nanocomposite.

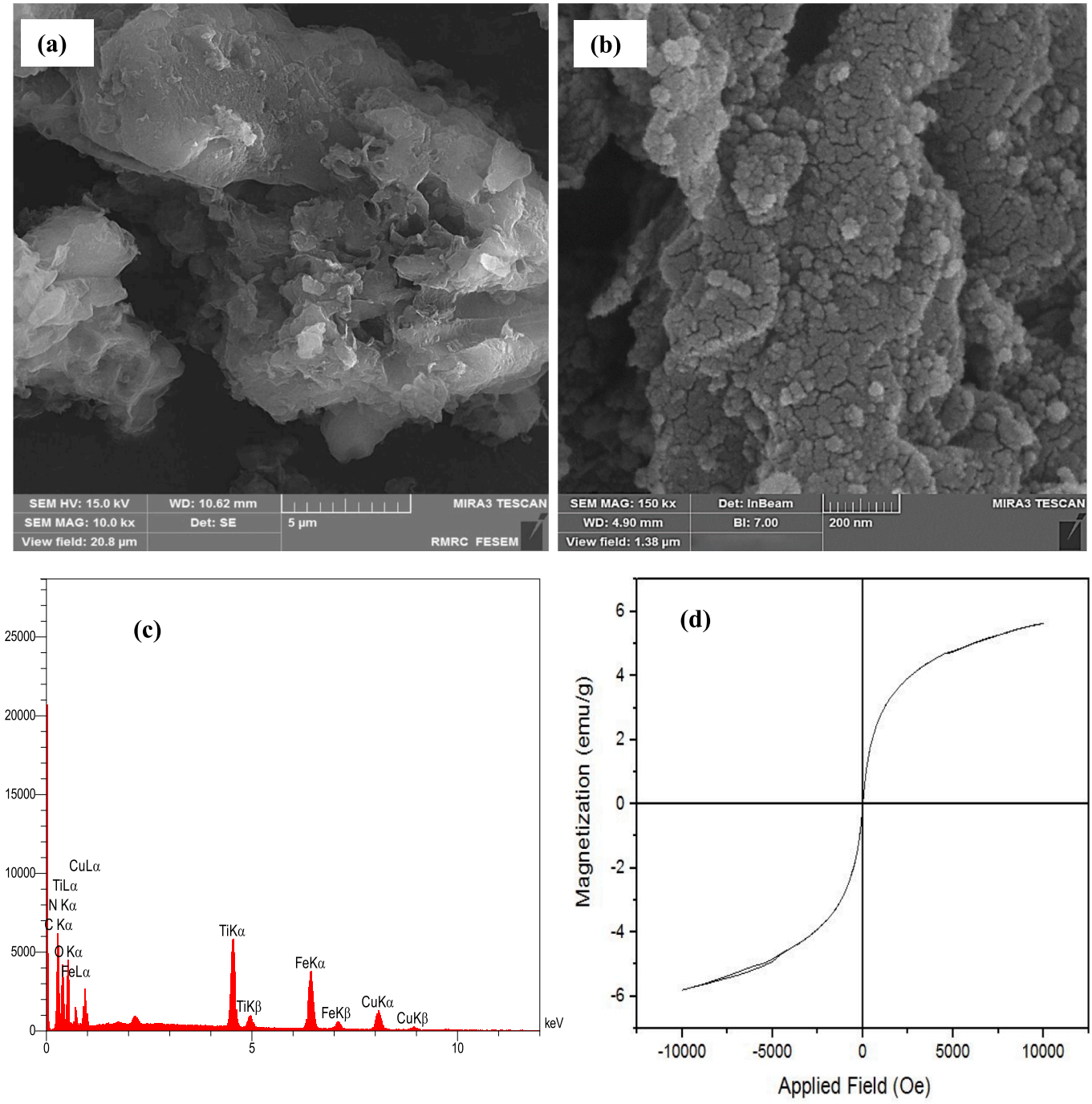

Fig. 2. FE-SEM image g-C_3N_4 (a), and g-C_3N_4/TiO_2/$CuFe_2O_4$ nanocomposite (b), EDS spectrum, of g-C_3N_4/TiO_2/$CuFe_2O_4$ nanocomposite (c), and magnetization curve of g-C_3N_4/TiO_2/$CuFe_2O_4$ nanocomposite (d).

of g-C_3N_4/TiO_2, TiO_2/$CuFe_2O_4$, and g-C_3N_4/$CuFe_2O_4$ confirm the successful synthesize of these nanocomposits (Fig. S1).

The FTIR technique was used to determine the surface functional group of the samples and the obtained spectra were displayed in the Fig. 1b. In the spectra of all the synthesized samples, the absorption bands at around 3320 and 1650 cm^{-1} are corresponded to stretching and bending vibrations of OH groups, respectively. In the case of TiO_2, the strong absorption bands at 500–800 cm^{-1} are related to Ti–O and Ti–O–Ti bonds stretching vibration. For pure $CuFe_2O_4$, the absorption peaks at 450 and 580 cm^{-1} are related to the stretching vibrations of metal–oxygen within the octahedral (Cu–O) and tetrahedral (Fe–O) sites in spinel structures, respectively. The FTIR spectrum of g-C_3N_4 has revealed absorption bands at 1239 cm^{-1}, 13121 cm^{-1}, 1411 cm^{-1}, and 1578 cm^{-1} which were related to the C-N aromatic stretching vibration. Furthermore, the peaks around 807, and1637 cm^{-1} are related to the tris-triazine units and C═N stretching vibrations. Moreover, all the characteristic absorption bands of TiO_2, g-C_3N_4, and $CuFe_2O_4$ were coexisted in the FTIR spectrum of g-C_3N_4/TiO_2/$CuFe_2O_4$ nanocomposite, which confirmed the successful preparation of the ternary nanocomposite.

The morphology and microstructure of the synthesized g-C_3N_4 as well as g-C_3N_4/TiO_2/$CuFe_2O_4$ nanocomposite were analyzed by FESEM and the images were depicted in Fig. 2. According to the Fig. 2a, g-C_3N_4 was shown the layered nanostructures containing nanosheets with wrinkle. Fig. 2b was exhibited that the TiO_2 nanoparticles and $CuFe_2O_4$

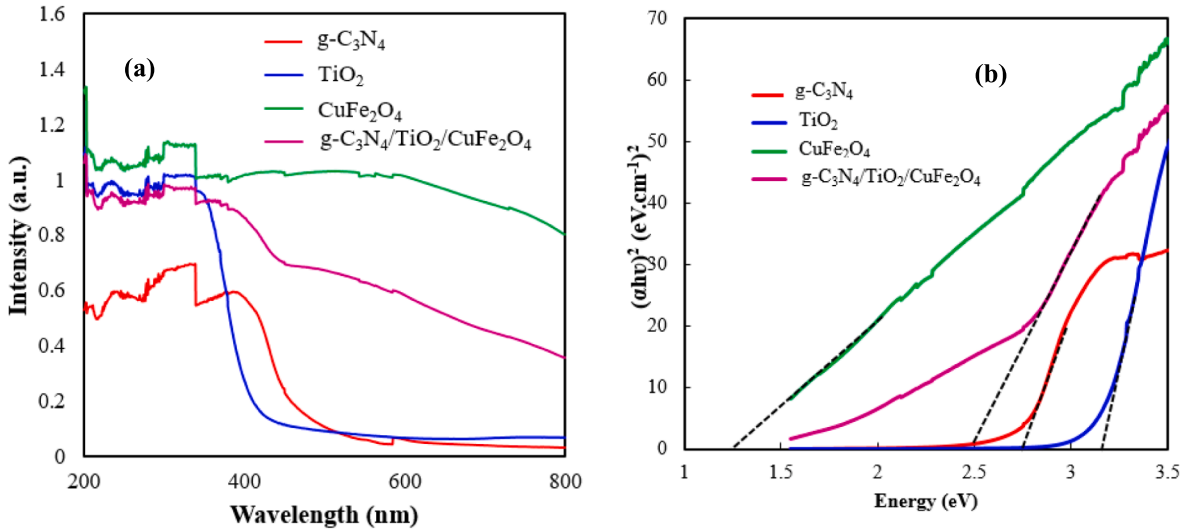

Fig. 3. Diffuse reflectance spectra (a), Tauc's plots (b) of g-C_3N_4, TiO_2, $CuFe_2O_4$, and g-C_3N_4/TiO_2/$CuFe_2O_4$ nanocomposite.

Table 3
ANOVA results of the quadratic model.

Source	Sum of Squares	df	Mean Square	F Value	p-value	
Model	3679.47	14	262.82	57.48	< 0.0001	significant
A-Dosage	1072.94	1	1072.94	234.66	< 0.0001	
B-Concentration	398.94	1	398.94	87.25	< 0.0001	
C-Time	329.37	1	329.37	72.04	< 0.0001	
D-pH	407.80	1	407.80	89.19	< 0.0001	
AB	0.65	1	0.65	0.14	0.7110	
AC	1.52	1	1.52	0.33	0.5729	
AD	0.85	1	0.85	0.19	0.6723	
BC	1.62	1	1.62	0.35	0.5606	
BD	1.82	1	1.82	0.40	0.5381	
CD	0.31	1	0.31	0.068	0.7979	
A^2	271.60	1	271.60	59.40	< 0.0001	
B^2	682.77	1	682.77	149.33	< 0.0001	
C^2	377.64	1	377.64	82.59	< 0.0001	
D^2	708.67	1	708.67	155.00	< 0.0001	
Residual	68.58	15	4.57			
Lack of Fit	40.14	10	4.01	0.71	0.7018	not significant
Pure Error	28.44	5	5.69			
Cor Total	3748.06	29				

nanoparticles were anchored on the surface of g-C_3N_4 nanosheets after combining these three nanomaterials and formation ternary nanocomposite. The EDS spectrum of g-C_3N_4/TiO_2/$CuFe_2O_4$ nanocomposite was represented in Fig. 2c, which reveals the presence of Ti, O, C, N, Cu, and Fe elements without any impurities in the synthesized nanocomposite.

The magnetic properties of g-C_3N_4/TiO_2/$CuFe_2O_4$ were investigated by VSM analysis. The VSM data (Fig. 2d) showed that the nanocomposite exhibits superparamagnetic behavior at room temperature with a weak ferromagnetic component. The magnetization (M) values of the nanocomposite increased as the magnetic field (H) was increased, indicating that the nanocomposite has ferromagnetic characteristics. At a magnetic field of 10 kOe, the saturation magnetization (Ms) value of g-C_3N_4/TiO_2/$CuFe_2O_4$ was found to be 5.62 emu/g.

Table 4
Statistical parameters for the proposed quadratic model by ANOVA.

R^2	0.9799
Adj. R^2	0.9722
Pred R^2	0.9417
C. V. %	2.47
PRESS	218.60

UV–Vis DRS analysis was used to investigate the optical properties of the as-prepared samples and the obtained results were exhibited in Fig. 3a. Pure TiO_2 was exhibited absorption in the ultraviolet region with the absorption edge of 390 nm. However, the absorption edge of g-C_3N_4, and $CuFe_2O_4$ were revealed at 450 and 880, which possess intensive absorption in the visible light region. Comparing to TiO_2, the ternary g-C_3N_4/TiO_2/$CuFe_2O_4$ nanocomposite was exhibited a red shift, which signify the final nanocomposite can response to visible light. The band gap energies of the as-synthesized samples were calculated using Tauc plot based on Kubelka-Munk function. According to Fig. 3b, the band gap energies of g-C_3N_4, TiO_2, $CuFe_2O_4$, and g-C_3N_4/TiO_2/$CuFe_2O_4$ were obtained 2.68, 3.15, 1.28 eV, and 2.45, respectively. Therefore, as a result g-C_3N_4/TiO_2/$CuFe_2O_4$ nanocomposite with intensive visible light absorption can form abundant photogenerated carriers, which lead to improve the photocatalytic performance.

3.2. *The model fitting and statistical analysis*

To optimize the photocatalytic activity of g-C_3N_4/TiO_2/$CuFe_2O_4$ for degradation of TC, four main influencing variables (dosage of photocatalyst, initial concentration of TC, reaction time and solution pH) were

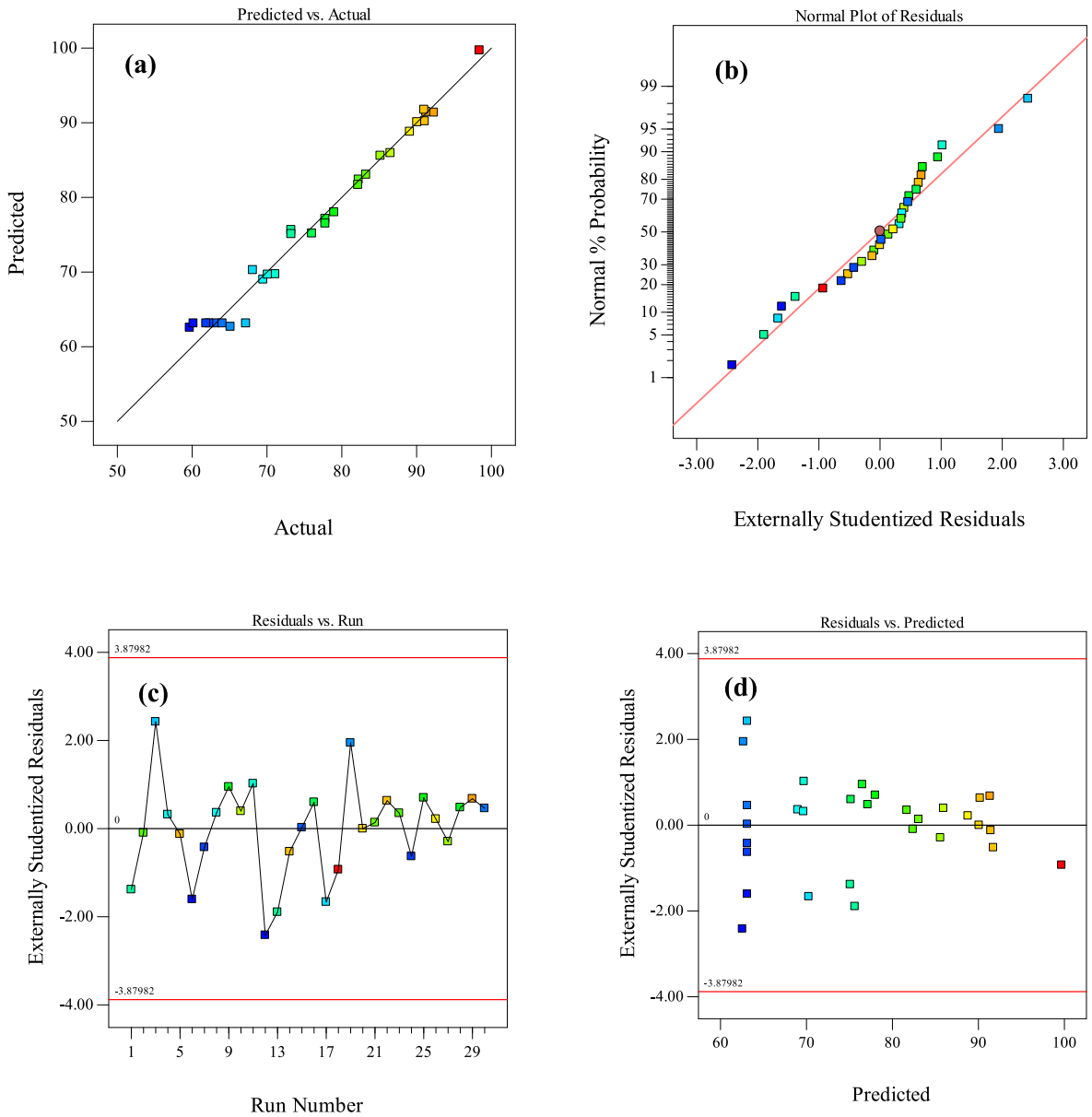

Fig. 4. Graphical plot of predicted versus actual values (a), normal probability plots of the residuals (b), externally studentized residuals versus predicted (c), and residuals versus run number (d) of the fitted model for photodegradation of TC by g-C_3N_4/TiO_2/$CuFe_2O_4$ nanocomposite.

optimized using RSM based CCD. The analysis of variance (ANOVA) was performed to investigate the adequacy and validity of the model and the results was shown in Table 3. Based on the analysis of variance (ANOVA) findings, it is evident that the proposed model and its constituent terms, namely A, B, C, D, A^2, B^2, C^2, and D^2, exhibit statistical significance, as indicated by their respective p-values being below 0.05, at a confidence level of 95%. Additionally, the p-value of the lack of fit is 0.7018, which demonstrate the lack of fit is not significant and the suggested model is adequate for predicting the TC degradation efficiency. As shown in Table 4, the high values of R^2 (0.9799), pred. R^2 (0.9722), and adj. R^2 (0.9417) show the excellent fitness between the predicted and experimental result. Further, with the reduce in the difference between R^2, pred. R^2, and adj. R^2 values, the entering chance non-significant terms in the suggested model is declined. Moreover, the coefficient of variation (C.V. %) value is low (2.47), which demonstrate good reliability of the experimental data. Also the value of predicted residual error sum of square (PREES = 218.60) is low reveals that the proposed model can successfully fit the data. The RSM results proposed the following second-order polynomial model in terms of coded factors:

$$\%R = 63.1333 + 6.68625\,A + -4.07708B + 3.70458C + -4.12208\,D + 3.14677\,A^2 + 4.98927\,B^2 + 3.71052\,C^2 + 5.08302\,D^2$$

The actual against predicted responses plot (Fig. 4a) was shown the closeness of actual values to predicted values. Therefore, the model can successfully predict the degradation efficiency of TC. The residual graphs in various modes containing normal probability plot, residuals vs. run number, and residuals vs. predicted were applied to investigate the adequacy of the model and the results was shown in Fig. 4b–d. As per the normal probability plot analysis, it is observed that the data points closely conform to a straight line, indicating that the residuals follow a normal distribution. (Dan et al., 2021). Additionally, the data points in the residuals vs. run number, and residuals vs. predicted plots are randomly scattered without any pattern. These results confirm the adequacy of the proposed model.

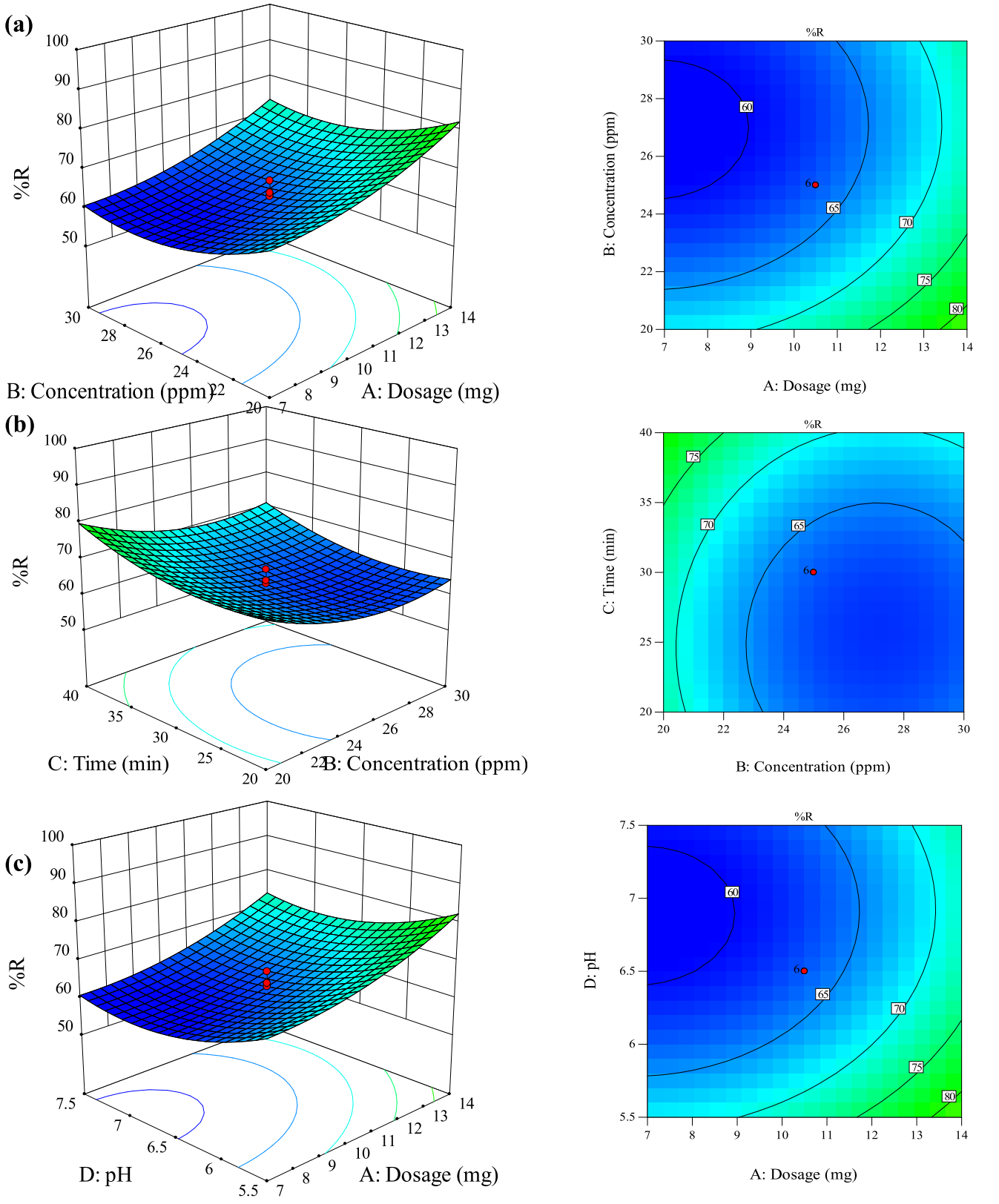

Fig. 5. Surface (3D) and contour (2D) plots for TC photodegradation by g-C_3N_4/TiO_2/$CuFe_2O_4$ nanocomposite.

3.3. Response surface analysis

The surface and contour plots were applied to visualize the effect of interactions of factors on the degradation of TC and the obtained results were depicted in Fig. 5. The interaction between TC concentration and photocatalyst dosage was presented in Fig. 5a. The results were shown a considerable enhancement in the photocatalytic degradation efficiency of TC with the rise in the photocatalyst dosage. This enhancement trend

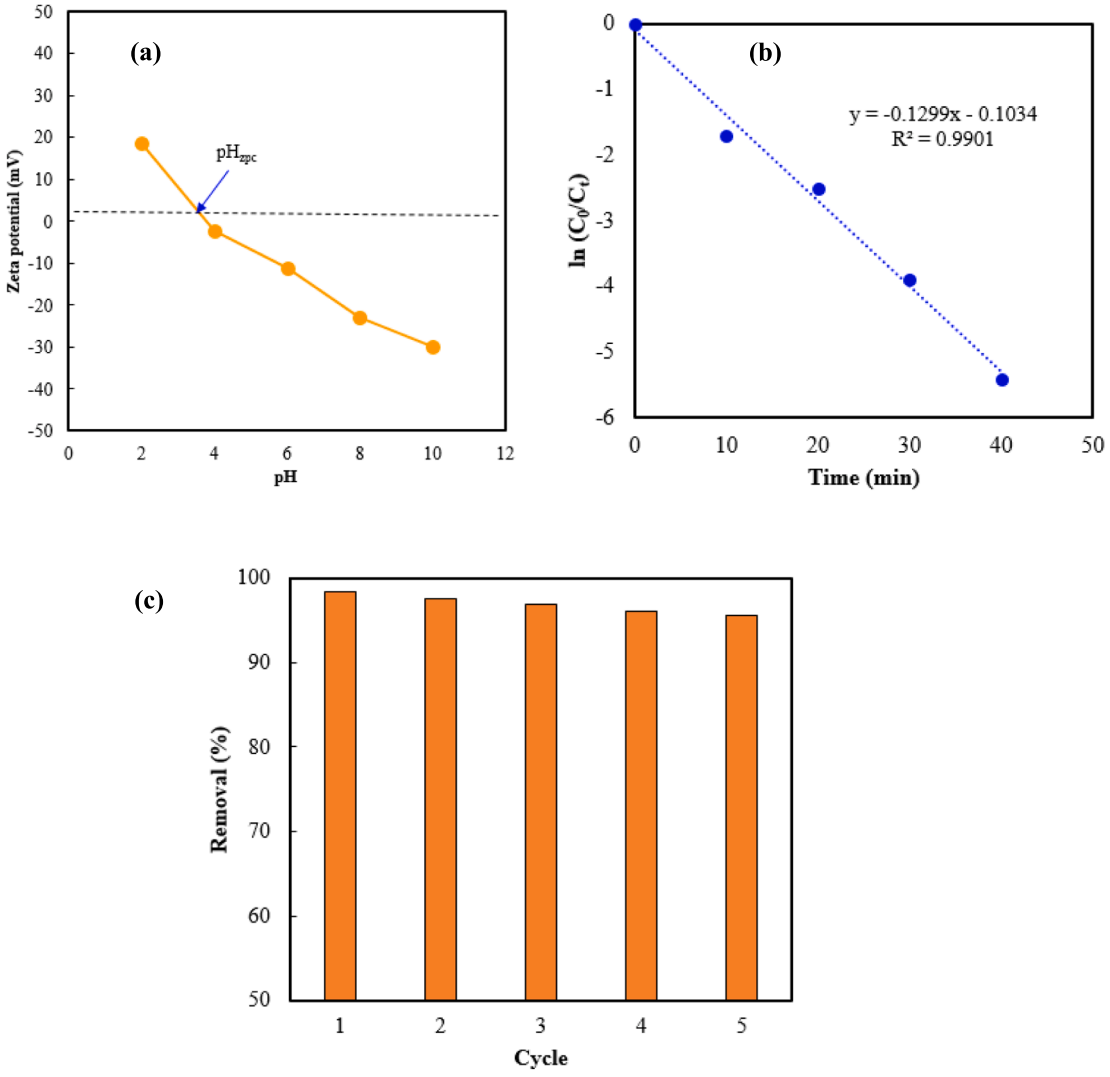

Fig. 6. Zeta potential of g-C_3N_4/TiO_2/$CuFe_2O_4$ nanocomposite (a), the corresponding kinetic of TC photodegradation (b), and Comparison of photocatalytic performance of various samples (c).

might be due to the increase in the active sites and adsorption capacity, which increase the photodegradation of adsorbed TC. Also, it is observed in this Figure that increasing in the initial concentration of TC lead to decline in the degradation efficiency due to unavailability of active sites and radical species in the high TC concentration. The influence of dosage of photocatalyst and time of irradiation was presented in Fig. 5b. The results demonstrate that the photocatalytic degradation percentage was increased by enhancement in the irradiation time, because increasing in the time leads towards the completion of degradation reaction. In fact, by increasing the irradiation time, the photocatalyst and pollutant have more opportunity to participate in the degradation reaction. Fig. 5c was shown the effect of TC concentration and solution pH. Regarding the effect of the pH of solution, it is clear that the degradation efficiency was increased with the increase of solution pH from 4.5 to 5.5 and at higher values, the degradation efficiency was decreased. It can be explained by zeta potential of g-C_3N_4/TiO_2/$CuFe_2O_4$ nanacomposite (Fig. 6a) and TC species distribution at different pHs of solution. The pH_{zpc} of g-C_3N_4/TiO_2/$CuFe_2O_4$ nanacomposite was 3.79, revealing that nanocomposite surface was positively charged at pH more than 3.79, and negatively charged at pH less than 3.79 [37].On the contrary, the prevalent form of TC within the pH range of 3.3 to 7.7 predominantly consists of TC^{o} molecules. This particular pH range facilitates conditions where the interaction between the nanocomposite material and TC molecules

Table 5
Results of RSM optimization.

Response	Parameter A (mg)	B (ppm)	C (min)	D	Predict response value	Experimental response value
%R	13.99	20.01	39.95	5.5	98.47	98.08

experiences reduced adsorption resistance. Consequently, this weakening of adsorption resistance enhances the availability and accessibility of active sites located on the surface of the nanocomposite. These active sites, now more readily available, effectively catalyze the degradation reactions of TC molecules. Thus, the pH-dependent predominance of TC_o molecules contributes significantly to the facilitation of degradation processes on the surface of the nanocomposite material. At the pH > 7.7, predominant TC species contain TCH^{-} and TC^{2-} and the degradation efficiency was declined due to charge repulsion between nanocomposite with negatively charged and molecules of TC [37].

Typically, the final step in experimental design is optimization of conditions. In this study, as shown in Table 5, the degradation efficiency of 98.47 % was suggested by the software under optimum conditions (photocatalyst dosage of 13.99 mg, TC concentration of 20.01 $mg.L^{-1}$ and at solution pH of 5.5 and during the course of 39.95 min reaction

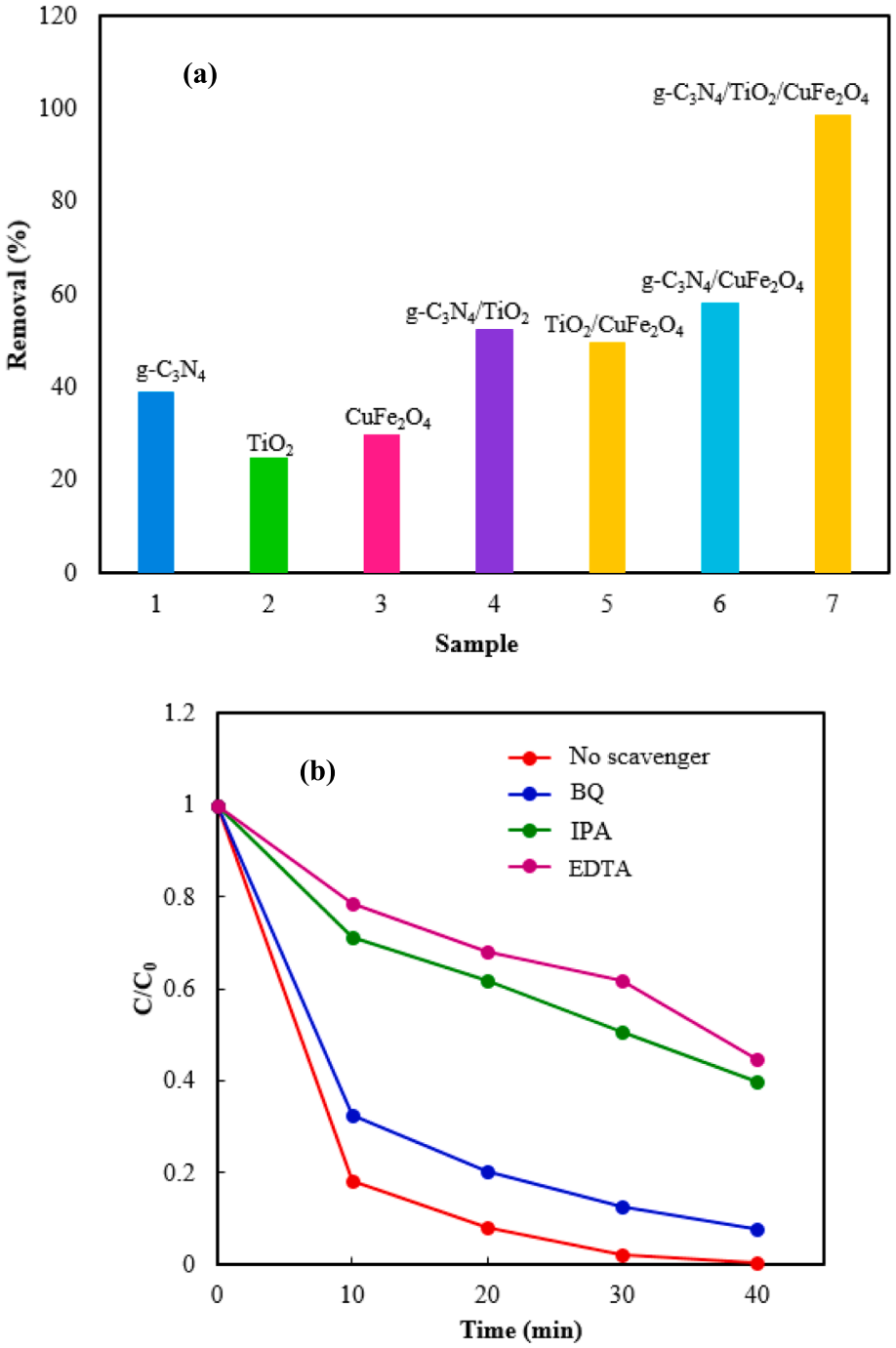

Fig. 7. Effect of various scavengers on TC photodegradation over g-C_3N_4/TiO_2/$CuFe_2O_4$.

time). Preforming an experiment under inclusion of optimal conditions yielded the TC photodegradation efficiency of 98.08 %, being in good assert with the predicted photodegradation percentage and revealing the accuracy of the suggested RSM model.

3.4. Kinetics study

The kinetic study of the involved photocatalytic process was performed based on Langmuir-Hinshelwood's model. According to this model, the heterogeneous photodegradation process rate follows pseudo-first-kinetic model:

$$\ln (C_0/C_t) = k_{app}\, t$$

In which C_0 (mg.L^{-1}), and C_t (mg.L^{-1}) indicate the initial concentration of TC and the concentration of TC after light illumination, respectively. Also, k_{app} (min^{-1}) and t (min) refer to apparent rate constant and the time of light illumination. Fig. 6b was shown the kinetic results considering to g-C_3N_4/TiO_2/$CuFe_2O_4$ photocatalysts. As Fig. 6b presents, the degradation of TC follows the pseudo-first-kinetic model. Furthermore, the k_{app} values for g-C_3N_4/TiO_2/$CuFe_2O_4$ was obtained 0.1013 min^{-1}.

3.5. Stability of g-C_3N_4/TiO_2/$CuFe_2O_4$

In addition to desirable phtocatalytic degradation efficiency, the photocatalyst stability is important criterions to appraise a

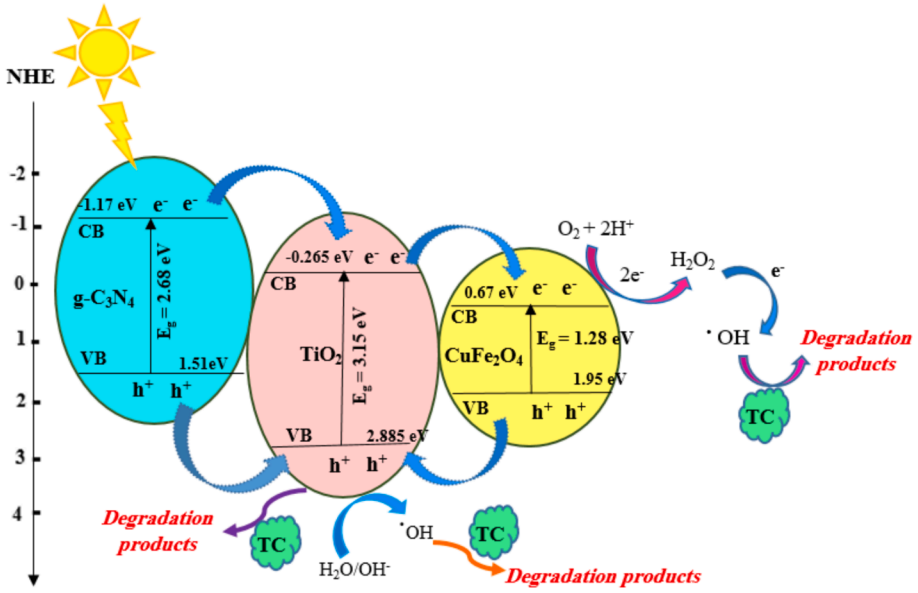

Fig. 8. Schematic diagram of TC photodegradation mechanism over g-C_3N_4/TiO_2/$CuFe_2O_4$ under visible light irradiation.

photocatalyst. Therefore, the reusability of the g-C_3N_4/TiO_2/$CuFe_2O_4$ nanocomposite was evaluated for 5 cycles under optimum conditions using circulation experiments. As shown in Fig. 6c, no significant decrease was observed in the photocatalytic efficiency after 5 cycles, which confirm the excellent stability of g-C_3N_4/TiO_2/$CuFe_2O_4$ nanocomposite.

3.6. Comparison of photocatalytic activity of various samples

The photocatalytic performance of g-C_3N_4/TiO_2/$CuFe_2O_4$ was compared with TiO_2, g-C_3N_4, $CuFe_2O_4$, g-C_3N_4/TiO_2, TiO_2/$CuFe_2O_4$, and g-C_3N_4/$CuFe_2O_4$ under optimal condition and the obtained results was shown in Fig. 7a. Notably, the g-C_3N_4/TiO_2/$CuFe_2O_4$ was exhibited the highest TC degradation activity after 40 min, which indicate the better photocatalytic activity of g-C_3N_4/TiO_2/$CuFe_2O_4$ compared to the TiO_2, g-C_3N_4, $CuFe_2O_4$, g-C_3N_4/TiO_2, and TiO_2/$CuFe_2O_4$. Therefore, the coupling of TiO_2, g-C_3N_4, and $CuFe_2O_4$ and the refinement of nanocomposite structure resulted in substantial advancements in both electron-hole pair separation and visible light absorption. This was achieved through precise design and engineering, enabling efficient management of charge carrier mobility. Moreover, the optimized nanocomposite architecture facilitated enhanced light absorption across the visible spectrum, thereby ensuring increased utilization of solar energy for photocatalytic applications.

3.7. Photocatalytic mechanism

In order to determine the main reactive species responsible for the photodegradation of TC by g-C_3N_4/TiO_2/$CuFe_2O_4$, radical trapping experiments were performed. Benzoquinone (BQ), isopropanol (IPA), and disodium ethylenediaminetetraacetic acid (EDTA-2Na) were used for trapping $\bullet O_2^-$, •OH, and h^+, respectively. As shown in Fig. 7b, after addition of EDTA-2Na and IPA to the solution, degradation efficiency was decreased, while addition of BQ has no significant influence on the TC photodegradation efficiency. Briefly, the radical trapping experiments reveal that the main reactive species responsible for degradation process of TC was in the order of $\bullet OH > h^+ > \bullet O_2^-$.

According to the above trapping experiments results, Eg, relative potentials of the conduction band (E_{CB}) and valance band (E_{VB}) of samples, a possible photocatalytic mechanism for photodegradation of TC by g-C_3N_4/TiO_2/$CuFe_2O_4$ was proposed and presented in Fig. 8. After visible light absorption by photocatalyst, $e^-$and h^+ were generated in the CB and VB of TiO_2, g-C_3N_4, and $CuFe_2O_4$. According to the energy diagram (Fig. 8), the photogenerated electrons from the CB of g-C_3N_4 spontaneously move to the CB of TiO_2, and then from the CB of TiO_2 move to the CB of $CuFe_2O_4$. Furthermore, the holes remain in the VB of TiO_2 and can participate directly in the degradation reaction of TC. Also, the E_{VB} of TiO_2 is more positive than the standard redox potentials of $OH^-/\bullet OH$ (1.99 eV vs. NHE) and $H_2O/\bullet OH$ (2.37 eV vs. NHE), which indicate the holes can react with OH^- or H_2O to generate •OH. The E_{CB} of $CuFe_2O_4$ is more positive than the standard redox potential of $O_2/\bullet O_2^-$ (−0.33 eV vs. NHE), which indicated the electrons in the CB of $CuFe_2O_4$ cannot reduce the O_2 on the surface of the photocatalyst to $\bullet O_2^-$ species. The CB of $CuFe_2O_4$ is more negative than the standard redox potential (O_2/H_2O_2) (0.685 eV vs. NHE).So, the electrons in the CB of $CuFe_2O_4$ could be trapped by absorbed O_2 and H^+ in the solution to form H_2O_2 species. Then, the H_2O_2 react with electrons and produce •OH species to participate in the TC photodegradation reaction.

4. Conclusion

In this study, the novel magnetic ternary g-C_3N_4/TiO_2/$CuFe_2O_4$ nanocomposite was fabricated via wet impregnation method. The as-synthesized nanocomposite was shown significantly enhanced photocatalytic activity for degradation of TC under visible light illumination. More importantly, the TC photodegradation by g-C_3N_4/TiO_2/$CuFe_2O_4$ nanocomposite has attained higher photodegradation efficiency, which is much higher than that of pristine TiO2, g-C_3N_4, $CuFe_2O_4$, and binary g-C_3N_4/TiO_2, TiO_2/$CuFe_2O_4$, and g-C_3N_4/$CuFe_2O_4$ nanocomposites. Notably, the extended optical absorption, and high electron/hole separation improve the photocatalytic degradation efficiency of TC by g-C_3N_4/TiO_2/$CuFe_2O_4$ nanocomposite. Moreover, CCD-RSM was applied to investigate the effect of operational parameters on the TC photodegradation efficiency. Complete photodegradation of TC occurred under the conditions of 13.99 mg nanocomposite, 20.01 $mg.L^{-1}$ TC, and pH 5.5, within 40 min. According to the scavenging experiments, holes and hydroxyl radicals were dominant species in the degradation process. This study indicates that the nanocomposite of g-C_3N_4/TiO_2/$CuFe_2O_4$ may be expected to be a promising candidate for removal of TC from aqueous solution.

CRediT authorship contribution statement

Khalid Mujasam Batoo: Writing – review & editing, Resources, Project administration, Investigation, Funding acquisition, Data curation, Conceptualization. **Kadhim Hussein Jassim:** Writing – review & editing, Visualization, Validation, Software, Methodology, Formal analysis, Data curation. **Talal Aziz Qassem:** Writing – review & editing, Validation, Supervision, Project administration, Funding acquisition, Data curation, Conceptualization. **Sajjad Hussain:** Writing – original draft, Software, Resources, Methodology, Investigation, Formal analysis. **Wafaa Talib Hasson:** Writing – original draft, Software, Resources, Methodology, Investigation, Formal analysis, Data curation. **Sarah Salah Jalal:** Visualization, Validation, Software, Resources, Methodology, Investigation. **Montather F. Ramadan:** Writing – original draft, Software, Resources, Methodology, Investigation, Formal analysis, Data curation, Conceptualization. **Safaa Mustafa Hameed:** Writing – original draft, Visualization, Validation, Software, Data curation, Conceptualization. **Ahmed Hussien Alawadi:** Writing – review & editing, Visualization, Validation, Software, Resources, Data curation, Conceptualization. **Ali Alsaalamy:** Writing – review & editing, Visualization, Validation, Software, Methodology, Investigation, Formal analysis, Data curation.

Declaration of competing interest

The authors declare that they have no known competing financial interests or personal relationships that could have appeared to influence the work reported in this paper.

Acknowledgment

The author K M Batoo would like to thank Researchers Supporting Project No. (RSP2023R148), King Saud University, Riyadh, Saudi Arabia for the financial support.

Appendix A. Supplementary data

Supplementary data to this article can be found online at https://doi.org/10.1016/j.jscs.2024.101871.

References

[1] J. Zhu, J. Wang, J. He, L. Hu, Fabrication of CdS/ZnCr-LDH heterojunctions with enhanced of tetracycline hydrochloride photocatalytic degradation under visible light, Opt. Mater. 136 (2023) 113456.
[2] C. Xiao, J. Yuan, L. Li, N. Zhong, D. Zhong, Q. Xie, H. Chang, Y. Xu, X. He, M. Li, Photocatalytic synergistic biofilms enhance tetracycline degradation and conversion, Environ. Sci. Ecotechnology 14 (2023) 100234.
[3] S. Gong, W. Zhang, Z. Liang, Y. Zhang, T. Gan, H. Hu, Z. Huang, Construction of a $BaTiO_3$/tubular g-C_3N_4 dual piezoelectric photocatalyst with enhanced carrier separation for efficient degradation of tetracycline, Chem. Eng. J. 461 (2023) 141947.
[4] L. Yang, C. Yuan, X. Chen, W. Xue, G. Cao, S. Meng, L. Bai, The effect of nitrification inhibitors on the aerobic biodegradation of tetracycline antibiotics in swine wastewater, Chemosphere 311 (2023) 136849.
[5] Y. Dou, X. Cheng, M. Miao, T. Wang, T. Hao, Y. Zhang, Y. Li, X. Ning, Q. Wang, The impact of chlorination on the tetracycline sorption behavior of microplastics in aqueous solution, Sci. Total Environ. 849 (2023) 157800.
[6] X. Wang, B. Zhang, J. Ma, P. Ning, Novel synthesis of aluminum hydroxide gel-coated nano zero-valent iron and studies of its activity in flocculation-enhanced removal of tetracycline, J. Environ. Sci. 89 (2020) 194–205.
[7] W. Zhang, Z. Bian, Y. Peng, H. Tang, H. Wang, Dual-function oxygen vacancy of BiOBr intensifies pollutant adsorption and molecular oxygen activation to remove tetracycline hydrochloride, Chem. Eng. J. 451 (2023) 138731.
[8] M. Kaleem, L.A. Minhas, M.Z. Hashmi, H.M. Farooqi, R. Waqar, K. Kamal, R. S. Aljaluod, K.M. Alarjani, A.S. Mumtaz, Biogenic synthesis of iron oxide nanoparticles and experimental modeling studies on the removal of heavy metals from wastewater, J. Saudi Chem. Soc. 28 (1) (2024) 101777.
[9] S. Dan, M. Kalantari, A. Kamyabi, M. Soltani, Synthesis of chitosan-g-itaconic acid hydrogel as an antibacterial drug carrier: optimization through RSM-CCD, Polym. Bull. 1–24 (2021).
[10] Y. Zhang, J. Zhou, X. Chen, L. Wang, W. Cai, Coupling of heterogeneous advanced oxidation processes and photocatalysis in efficient degradation of tetracycline hydrochloride by Fe-based MOFs: synergistic effect and degradation pathway, Chem. Eng. J. 369 (2019) 745–757.
[11] H. Sun, F. Guo, J. Pan, W. Huang, K. Wang, W. Shi, One-pot thermal polymerization route to prepare N-deficient modified g-C_3N_4 for the degradation of tetracycline by the synergistic effect of photocatalysis and persulfate-based advanced oxidation process, Chem. Eng. J. 406 (2021) 126844.
[12] C. Lai, F. Xu, M. Zhang, B. Li, S. Liu, H. Yi, L. Li, L. Qin, X. Liu, Y. Fu, N. An, Facile synthesis of CeO_2/carbonate doped $Bi_2O_2CO_3$ Z-scheme heterojunction for improved visible-light photocatalytic performance: photodegradation of tetracycline and photocatalytic mechanism, J. Colloid Interface Sci. 588 (2021) 283–294.
[13] F.D. Wu, J.C. Chen, J.P. Hu, Synthesis of TiO_2/Ti_3C_2Tx/AgI Z-scheme photocatalyst for tetracycline hydrochloride photocatalytic degradation, J. Environ. Chem. Eng. 10 (2022) 107117.
[14] S. Wang, L. Zhao, L. Gao, D. Yang, S. Wen, W. Huang, Z. Sun, J. Guo, X. Jiang, C. Lu, Fabrication of ternary dual Z-Scheme AgI/$ZnIn_2S_4$/$BiVO_4$ heterojunction photocatalyst with enhanced photocatalytic degradation of tetracycline under visible light, Arab. J. Chem. 15 (2022) 104159.
[15] H. Mirhosseini, A. Mostafavi, T. Shamspur, Highly efficient $LaFeO_3/Bi_2WO_6$ Z-scheme nanocomposite for photodegradation of tetracycline under visible light irradiation: statistical modeling and optimization of process by CCD-RSM, Mater. Sci. Semicond. Process. 160 (2023) 107413.
[16] D. Chen, Y. Cheng, N. Zhou, P. Chen, Y. Wang, K. Li, S. Huo, P. Cheng, P. Peng, R. Zhang, L. Wang, Photocatalytic degradation of organic pollutants using TiO_2-based photocatalysts: a review, J. Clean. Prod. 268 (2020) 121725.
[17] C. Luo, X. Ren, Z. Dai, Y. Zhang, X. Qi, C. Pan, Present perspectives of advanced characterization techniques in TiO_2-based photocatalysts, ACS Appl. Mater. Interfaces 9 (2017) (2017) 23265–23286.
[18] M. Zeshan, I.A. Bhatti, M. Mohsin, M. Iqbal, N. Amjed, J. Nisar, N. AlMasoud, T. S. Alomar, Remediation of pesticides using TiO_2 based photocatalytic strategies: a review, Chemosphere 300 (2022) 134525.
[19] Q. Shi, Y. Zhang, D. Sun, S. Zhang, T. Tang, X. Zhang, S. Cao, Bi_2O_3-sensitized TiO_2 hollow photocatalyst drives the efficient removal of tetracyclines under visible light, Inorg. Chem. 59 (2020) 18131–18140.
[20] R.S. Sutar, R.P. Barkul, S.D. Delekar, M.K. Patil, Sunlight assisted photocatalytic degradation of organic pollutants using g-C_3N_4-TiO_2 nanocomposites, Arab. J. Chem. 13 (2020) 4966–4977.
[21] H. Mirhosseini, A. Mostafavi, T. Shamspur, G. Sargazi, Fabrication of an efficient ternary TiO_2/Bi_2WO_6 nanocomposite supported on g-C_3N_4 with enhanced visible-light-photocatalytic activity: modeling and systematic optimization procedure, Arab. J. Chem. 15 (2022) 103729.
[22] E. Kusiak-Nejman, A.W. Morawski, TiO_2/graphene-based nanocomposites for water treatment: a brief overview of charge carrier transfer, antimicrobial and photocatalytic performance, Appl. Catal. B Environ. 253 (2019) 179–186.
[23] M. Ismael, A review on graphitic carbon nitride (g-C3N4) based nanocomposites: synthesis, categories, and their application in photocatalysis, J. Alloys Compd. 846 (2020) 156446.
[24] E. Baladi, F. Davar, A. Hojjati-Najafabadi, Synthesis and characterization of g–C_3N_4–$CoFe_2O_4$–ZnO magnetic nanocomposites for enhancing photocatalytic activity with visible light for degradation of penicillin G antibiotic, Environ. Res. 215 (2022) 114270.
[25] F. Xie, G. Dong, M. Wu, K. Wu, C. Huang, S. Du, Y. Li, M. Wei, C. Chen, Iodine-doped g-C_3N_4 modified zinc titanate electron transporting layer for highly efficient perovskite solar cells, J. Colloid Interface Sci. 635 (2023) 159–166.
[26] Z. Zou, Z. Zhao, Z. Zhang, W. Tian, C. Yang, X. Jin, K. Zhang, Room-temperature optoelectronic gas sensor based on core-shell g-C3N4@ WO3 heterocomposites for efficient ammonia detection, Anal. Chem. 95 (2023) 2110–2118.
[27] Z. Liu, W. Guo, X. Liu, G. Wu, Y. Tang, Z. Mo, D. Yang, Study on photoelectric properties of Fe-Co codoped g-C_3N_4, Environ. Res. 200 (2021) 111736.
[28] H. Chen, Y. Xing, S. Liu, Y. Liang, J. Fu, L. Wang, W. Wang, Mechanistic insights into efficient photocatalytic H_2O_2 production of 2D/2D g-C_3N_4/In_2S_3 photocatalyst by tracking charge flow direction, Chem. Eng. J. 462 (2023) 142038.
[29] Q. Yang, T. Wang, Z. Zheng, B. Xing, C. Li, B. Li, Constructing interfacial active sites in Ru/g-C_3N_4– x photocatalyst for boosting H_2 evolution coupled with selective benzyl-alcohol oxidation, Appl. Catal. B Environ. 315 (2022) 121575.
[30] W. Liu, D. Zhang, R. Wang, Z. Zhang, S. Qiu, 2D/2D interface engineering promotes charge separation of Mo_2C/g-C_3N_4 nanojunction photocatalysts for efficient photocatalytic hydrogen evolution, ACS Appl. Mater. Interfaces 14 (2022) 31782–31791.
[31] P. Gündoğmuş, J. Park, A. Öztürk, Preparation and photocatalytic activity of g-C_3N_4/TiO_2 heterojunctions under solar light illumination, Ceram. Int. 46 (2022) 21431–21438.
[32] M. Rafieezadeh, A.H. Kianfar, Fabrication of heterojunction ternary Fe_3O_4/TiO_2/$CoMoO_4$ as a magnetic photocatalyst for organic dyes degradation under sunlight irradiation, J. Photochem. Photobiol. A Chem. 423 (2022) 113596.
[33] G. Palanisamy, K. Bhuvaneswari, G. Bharathi, T. Pazhanivel, M. Dhanalakshmi, Improved photocatalytic performance of magnetically recoverable Bi_2Te_3/CdS/$CuFe_2O_4$ nanocomposite for MB dye under visible light exposure, Solid State Sci. 115 (2021) 106584.
[34] X. Liu, J. Zhou, D. Liu, L. Li, W. Liu, S. Liu, C. Feng, Construction of Z-scheme $CuFe_2O_4/MnO_2$ photocatalyst and activating peroxymonosulfate for phenol degradation: synergistic effect, degradation pathways, and mechanism, Environ. Res. 200 (2022) 111736.

[35] K. Atacan, N. Güy, M. Ozacar, Design and synthesis of magnetically separable $CuFe_2O_4/MoS_2$ p-n heterojunction for photocatalytic effciency of Rhodamine B degradation, Colloid Interface Sci. Commun. 40 (2021) 100359.
[36] M. Golshan, B. Kakavandi, M. Ahmadi, M. Azizi, Photocatalytic activation of peroxymonosulfate by TiO2 anchored on cupper ferrite (TiO2@CuFe2O4) into 2,4-D degradation: process feasibility, mechanism and pathway, J. Hazard. Mater. 359 (2018) 325–337.
[37] Z. Mengting, T.A. Kurniawan, Y. Yanping, M.H.D. Othman, R. Avtar, D. Fu, G. H. Hwang, Fabrication, characterization, and application of ternary magnetic recyclable Bi_2WO_6/BiOI@ Fe_3O_4 composite for photodegradation of tetracycline in aqueous solutions, J. Environ. Manage. 270 (2020) 110839.